Case History

Seismic characterization of heavy oil reservoir during thermal production: A case study

Hemin Yuan[1], De-Hua Han[1], and Weimin Zhang[2]

ABSTRACT

Heavy oil reservoirs are important alternative energy resources to conventional oil and gas reservoirs. However, due to the high viscosity, most production methods of heavy oil reservoirs involve thermal production. Heavy oil reservoirs' properties change dramatically during thermal production because the viscosity drops drastically with increasing temperature. Moreover, the velocity and density also decrease after steam injection, leading to a longer traveltime of seismic velocities and low impedance of the steam chamber zone. These changes of properties can act as indicators of the steam chamber and can be detected through the time-lapse inversion method. We first establish the rock-physics relationship between oil sands' impedance and temperature on the basis of our previous laboratory work. Then, we perform the forward modeling of the heavy oil reservoir with the steam chamber to demonstrate the influence of steam injection on seismic profiles. Then, we develop a modified-Cauchy prior-distribution-based time-lapse inversion method and perform a 2D model test. The inversion method is then applied on the real field data, and the results are analyzed. By combining the inverted impedance and rock-physics relation between impedance and temperature, the temperature distribution map is obtained, which can work as an indicator of steam chamber. Finally, an empirical relation between impedance and velocity is established, and velocity is derived from the impedance.

INTRODUCTION

The heavy oil reservoir is one of the most important unconventional hydrocarbon resources, and its amount is almost three times that of the conventional oil reservoir (Meyer and Attanasi, 2003). Heavy oil usually has a very high viscosity that could be more than 1,000,000 cp (Meyer and Attanasi, 2003). Because of the high viscosity, heavy oil cannot be pumped out directly and many production methods involve injecting hot steam to reduce the viscosity. Among the thermal production methods, one important method is steam-assisted gravity drainage (SAGD) (Butler, 1990). It involves drilling a pair of wells: one for steam injection and the other for production. These two wells are separated 4–6 m apart, and the injection well is right above the production well. The steam from the top well will rise up, heat the reservoir, and generate a steam chamber (Butler, 1990). As the oil is heated, the viscosity drops and

becomes movable and then mixes with the water and steam, forming a mixture. Due to gravity, the mixture will flow downward to the production well, which can pump the mixture out. A schematic map of SAGD is displayed in Figure 1. Figure 1a shows the principle of SAGD, and Figure 1b shows a vertical view of a steam chamber. For field production, it is significant to know the size of the steam chamber, the remaining oil distribution, and the distribution of the temperature.

The properties of the steam chamber zone are distinct from the original in situ layers because the steam chamber is washed by hot steam and in situ layers keep the original properties. The in situ layers, which are filled with solid oil — owing to the high viscosity at low temperature — have a relatively stiff frame and high velocities (Yuan and Han, 2013b), whereas the steam chamber that is filled with a mixture of steam, water, and oil has very low velocities. The appearance of hot steam not only reduces the velocities, but

also reduces the density of the steam chamber (Bianco et al., 2008). Thus, the impedance of the steam chamber is lower compared with the in situ layers, which can lead to strong reflections on the top and bottom of the steam chamber.

Many people have done research on seismic characterization of heavy oil reservoirs (Eastwood et al., 1994; Isaac, 1996; Sun, 1999; Li et al., 2001; Nakayama et al., 2008; Dumitrescu and Lines, 2009; Kendall, 2009). Eastwood et al. (1994) use a time delay to detect the steam zone. Zhang et al. (2002) use the reflection image to show the monitored zone. The time difference and amplitude-anomaly method were also applied to simulate the production zone (Zou et al., 2004). Reflectivity change was also used to monitor the steam injection (Schmitt, 1999). Marcano (2013) adopts geochemical proxies to detect the steam zone. However, the conditions vary in different reservoirs, and there are few quantitative studies (Kato, 2010) on inverting the temperature distribution through the combination of the seismic inversion and the rock-physics relation. In this paper, we applied time-lapse inversion on the 4D-2D data with a modified-Cauchy prior constraint. Based on our previous laboratory work, the rock-physics relation between the oil sands' impedance and temperature was established. Then, the inversion results and rock-physics relation were combined to map the temperature distributions. Finally, by applying an empirical equation that links impedance and velocity, the velocity was also obtained.

METHODOLOGY

Heavy oil viscosity is highly temperature sensitive, and its moduli and velocities are also dependent on temperature. Consequently, the oil sands (heavy oil-saturated sands) also show temperature-dependent velocities. Moreover, as the oil viscosity drops, the oil in the pore space of oil sands can be washed and substituted by hot steam, leading to decreases of the velocity and density. Thus, the oil sands' impedance is also temperature dependent and it is significant to figure out the relationship between the oil sands' impedance and

Figure 1. Illustrations of (a) SAGD and (b) steam chamber. In SAGD, two horizontal wells are drilled: one for the steam-injection well on top and the other for the oil-production well on bottom. The hot steam injected from the top well will rise up and heat the reservoir, generating a steam chamber. Panel (b) shows the vertical view of the steam chamber. The steam of the reservoir will spread on top of the reservoir and flow downward by gravity; thus, it can be produced through the well on the bottom.
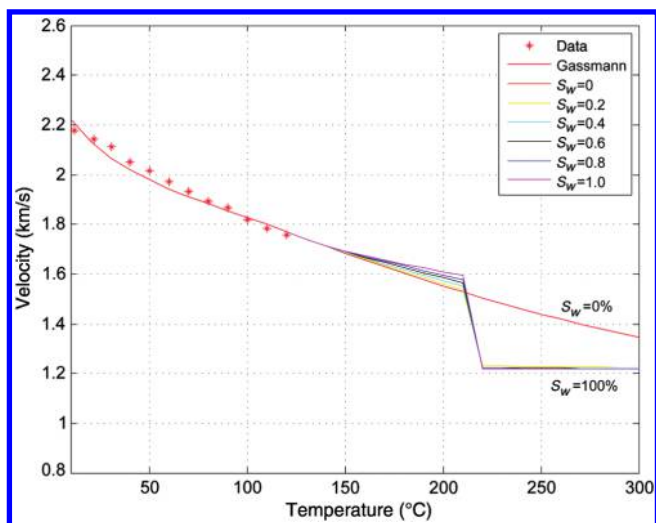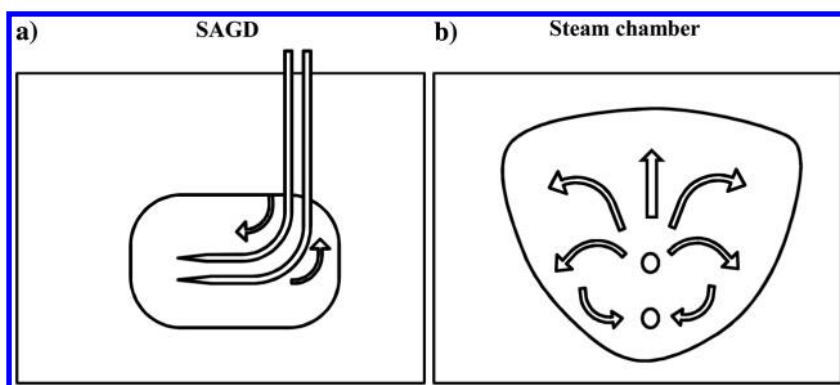

Figure 2. Heavy oil sands' velocity variations with temperature (from Yuan et al., 2016). The discrete red stars are the laboratory-measured data; the red lines correspond to water saturation of 0%; the yellow lines correspond to water saturation of 20%; the cyan lines correspond to water saturation of 40%; the black lines correspond to water saturation of 60%; the blue lines correspond to water saturation of 80%; and the mauve lines correspond to water saturation of 100%.
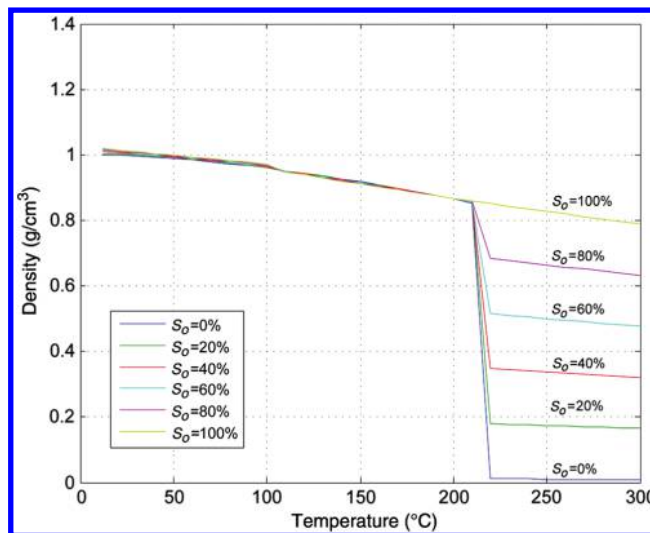

Figure 3. Density of the oil and water mixture under different temperatures (from Yuan et al., 2016). The blue lines correspond to oil saturation of 0%; the green lines correspond to oil saturation of 20%; the red lines correspond to oil saturation of 40%; the cyan lines correspond to oil saturation of 60%; the mauve lines correspond to oil saturation of 80%; and the yellow lines correspond to oil saturation of 100%.

temperature so that we can know how much influence temperature has on impedance.

Rock-physics relation

In our previous work, based on laboratory measurements, we have established the relationship between oil sands' velocities and temperature and the relationship between the temperature and the density of oil and water mixture (Yuan et al., 2016), as shown in
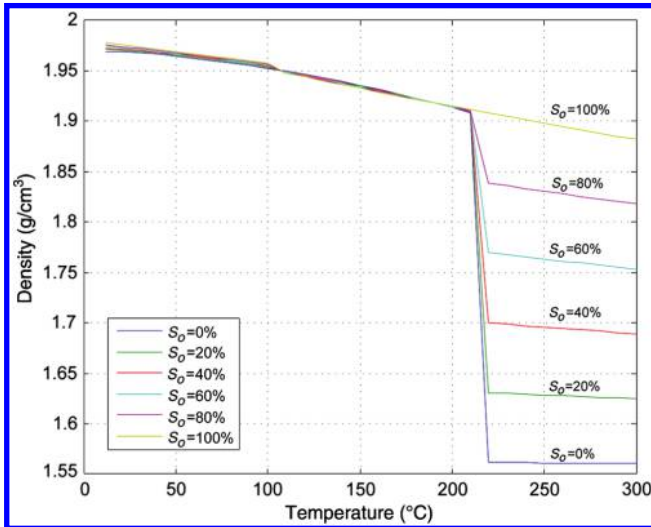

Figure 4. Density of oil sands under different temperatures. The blue lines correspond to oil saturation of 0%; the green lines correspond to oil saturation of 20%; the red lines correspond to oil saturation of 40%; the cyan lines correspond to oil saturation of 60%; the mauve lines correspond to oil saturation of 80%; and the yellow lines correspond to oil saturation of 100%.
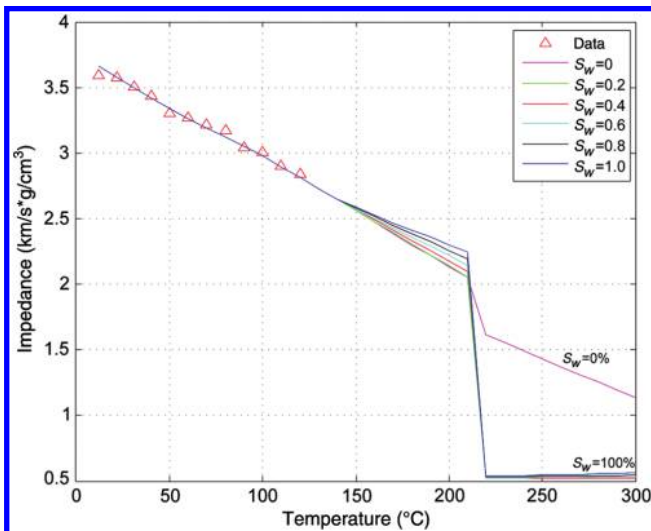

Figure 5. Impedance of oil sands under different temperatures. The blue lines correspond to water saturation of 100%; the green lines correspond to water saturation of 20%; the red lines correspond to water saturation of 40%; the cyan lines correspond to water saturation of 60%; and the black lines correspond to water saturation of 80%.
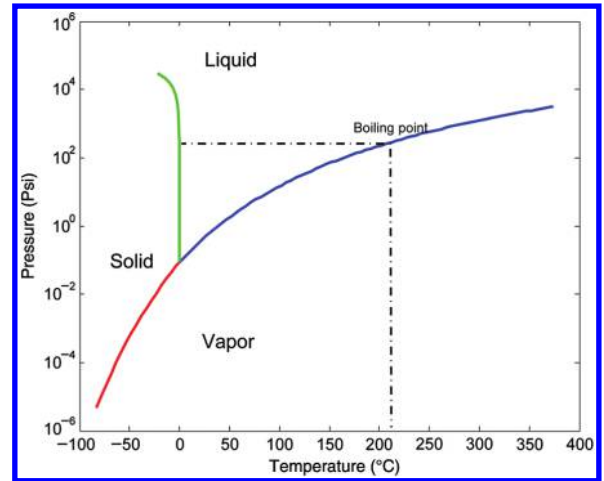

Figure 6. The phase diagram of water. The red line is the melting line; the blue line is the saturation line; and the green line is the sublimation line. The black point where the dashed line crosses the saturation line is the boiling point of the water under in situ pressure (334 psi). It indicates at what temperature the water turns to vapor in the steam chamber.

Table 1. The parameters of the geologic model. The information of each bed is derived from the well and seismic data provided by Cenovus Energy Inc. The density and velocity of the steam chamber are not available in the well logs, but they can be obtained through the laboratory measurement and calculations.

	Depth (m)	Density (g/cm^3)	Velocity (km/s)
Layer 1	0–186	2.024	2.309
Layer 2	186–190	2.221	2.067
Layer 3	190–215	2.216	2.157
Layer 4	215–242	2.024	2.309
Layer 5	242–258	2.047	2.400
Layer 6	258–263	2.033	3.634
Layer 7	263–298	2017	2.243
Layer 8	298–303	2.370	4.241
Layer 9	303–410	2072	2.494
Steam chamber	225–245	NA	NA

Table 2. The parameters of survey setup for forward modeling. The numbers of shots and receivers, the shot interval, and receiver interval are provided. The algorithm is based on finite-difference forward modeling, and the gridding information is provided.

	Parameters
Shots	7
Shot interval	90 m
Receivers	61
Receiver interval	10 m
Gridding	1 m

Figures 2 and 3. Because the porosity of the oil sands sample is known as 41.25% and the density of sand grains is known as 2.65 g/cm³, the densities of the oil sands can be derived through equation 1:

$$\rho_s = \rho_g(1 - \phi) + \rho_f\phi, \tag{1}$$

where ρ_s is the density of the oil sand, ρ_g is the grain density, ρ_f is the density of the fluid mixture, and ϕ is the porosity. The calculated densities of the oil sands are shown in Figure 4. With the densities and velocities, the impedance can be obtained. The derived impedance is shown in Figure 5.

In Figures 2, 4, and 5, the oil sands' velocity, density, and impedance show similar trends: They decrease with increasing temperature when the temperature is less than 210°C; they stay constant when the temperature is greater than 210°C; and they show dramatic drops at approximately 210°C because 210°C is the boiling point of the water under in situ pressure (334 psi), as shown in Figure 6. When the temperature is less than 210°C, the water in the pore space stays in a liquid state and the oil viscosity decreases with increasing temperature, causing the rock's velocity and impedance to decrease. When the temperature increases to 210°C, the water turns to vapor (steam), which has extremely low density and moduli, leading to a drastic drop in the bulk modulus of the fluid mixture. Because steam can substitute the oil in the pore space and can form isostress
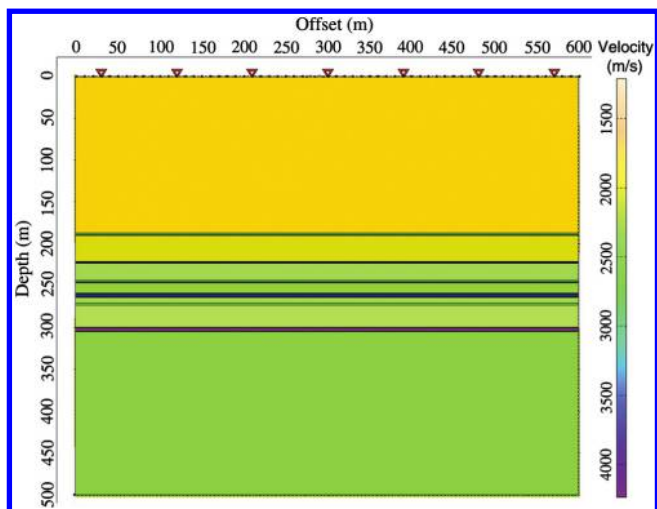

Figure 7. The geologic model before steam injection. The model is built based on well and seismic data provided by Cenovus Energy. The red triangles indicate the location of the source, and the dots are receivers. This model shows the initial conditions of the reservoir. It also shows the thickness and sequence of the geologic layers.
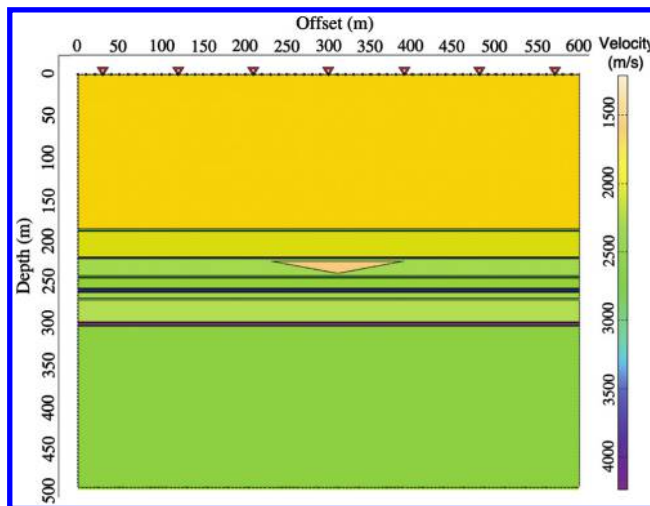

Figure 8. The updated geologic model with a steam chamber is indicated. The velocity of the oil sand is calculated with the Gassmann equation. This model shows the conditions of the reservoir after steam injection. It also shows the thickness and sequence of the geologic layers and the location and time depth of steam chamber.
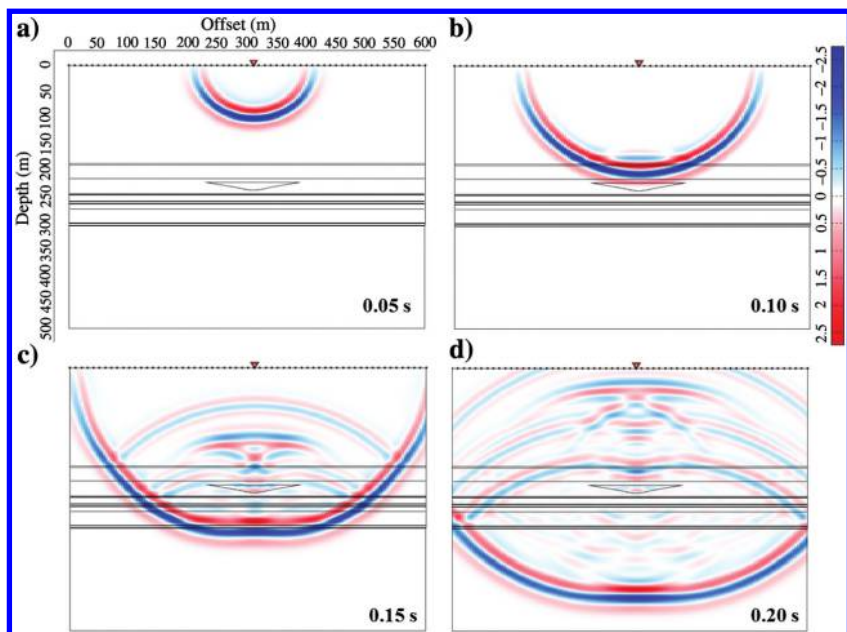

Figure 9. Snapshots of the wavefield. The number in the lower right corner indicates time. The successive snapshots indicate the wave propagations with time.

conditions with rock frame (Yuan et al., 2016), the density and bulk modulus of the rock drop intensely. As a result, the impedance of the oil sands displays a drastic drop. Physically, it is the hot steam heating the oil and substituting the oil that causes the velocity, density, and impedance of the rock to drop. The monotonic relation between impedance and temperature suggests that it can be derived through impedance.
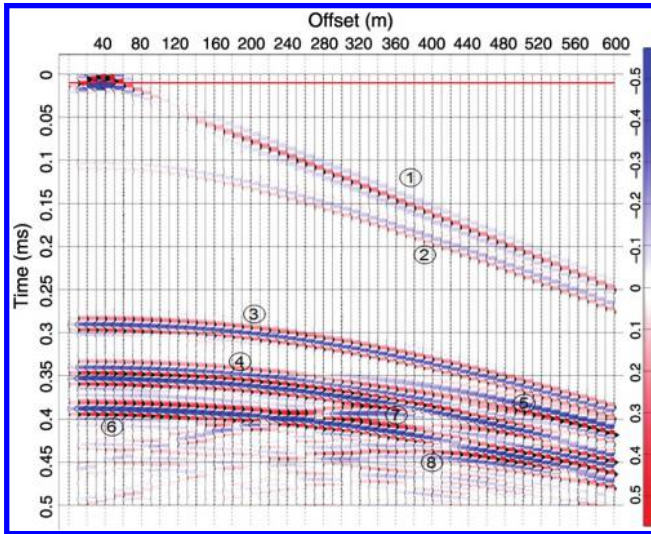

Figure 10. The generated angle gather of forward modeling. Here, ① is direct wave; ②, ③, ④, and ⑥ are reflection wave from different horizontal boundaries; ⑤ is the reflection wave from the top of the steam chamber; ⑦ and ⑧ are downgoing waves that are first reflected upward from the bottom of steam chamber, and then they are reflected downward from the top of the steam chamber.
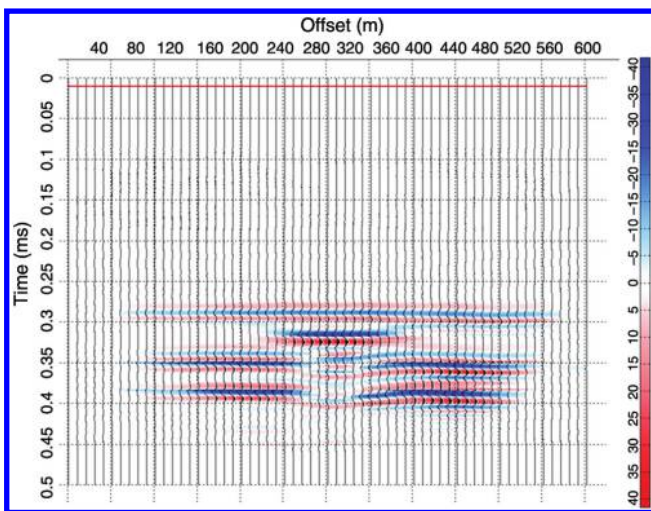

Figure 11. The result of forward modeling. This seismic profile is the migration result of the angle gathers. It shows the true events of the geologic layers. The strong reflections on the top and bottom of the steam chamber can be observed.

Forward modeling

To simulate the seismic energy spreading and study the seismic response of the heavy oil reservoir, especially after steam injection, forward modeling is indispensible. Forward modeling is a technique that can theoretically simulate the responses of geologic bodies. According to different theoretical basis, forward modeling can be divided into two types: ray-tracing and wave-equation methods. Because we want to study the influence of steam injection on the seismic wavefield, we use an acoustic-wave equation-based finite-difference algorithm to do the simulation (Diao et al., 2003), and the acoustic-wave equation in 2D space is in equation 2:
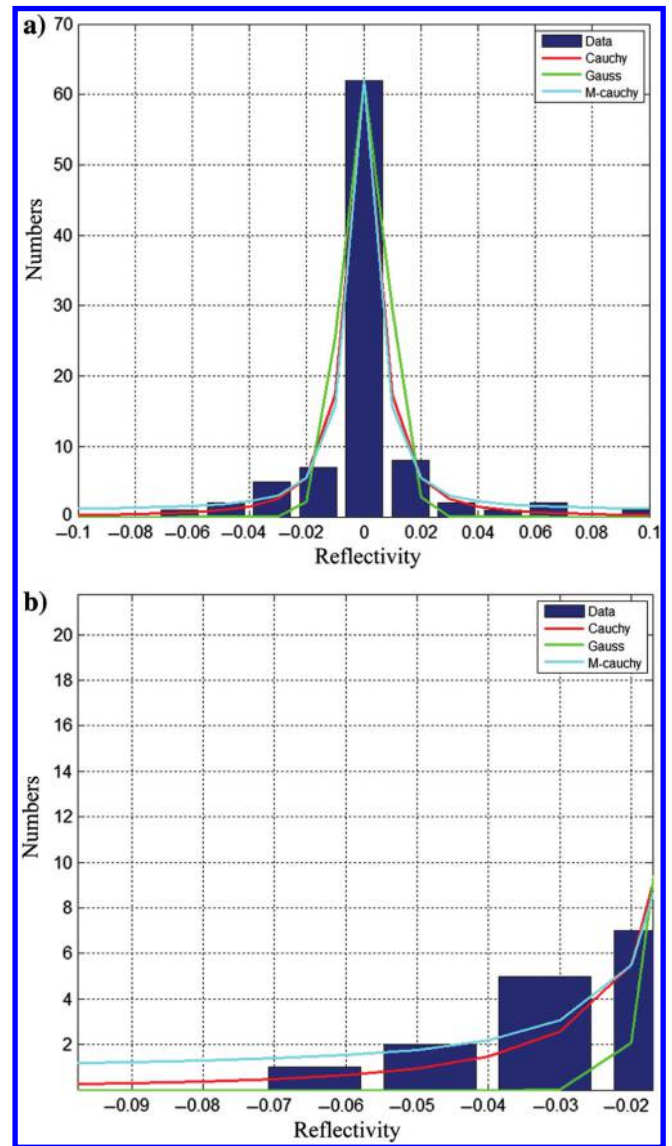

Figure 12. (a) The fit between the prior distributions and the histograms of statistical reflectivity. (b) The enlarged view of the distributions within reflectivity from −0.09 to −0.02. The blue bars represent the statistical reflectivities obtained from well logs; the green line represents the Gaussian distribution; the red line represents the Cauchy distribution; and the cyan line represents the modified-Cauchy distribution.

$$\frac{\partial^2 p}{\partial^2 t} - \rho c^2 \nabla \left(\frac{1}{\rho} \nabla p \right) = \delta(r) f(t), \qquad (2)$$

where $\delta(r)$ is the location of the source, $f(t)$ is the property of source at different times, p is the pressure field, c is the velocity, and ρ is the density.

Based on the information provided by Cenovus Energy Inc., a geologic model (before steam injection) is established (W. M. Zhang, personal communication, 2015). Table 1 shows the parameters of each bed that are derived from the well and seismic data. However, the density and velocity of the steam chamber are unknown.

We assume that the fluid inside the steam chamber is a mixture of oil, water, and steam; then the velocity and density of the steam chamber can be obtained from Figures 2 and 4 (the P-wave velocity is 1.21 km/s and the density is 1.63 g/cm^3). Figure 7 displays the original geologic model before steam injection, and Figure 8 shows the updated model with the steam chamber introduced. The parameters of the survey setup are shown in Table 2.

Then forward modeling can be performed. The snapshots of the wavefield are shown in Figure 9, the angle gather is shown in Figure 10, and the seismic profile after prestack depth migration is displayed in Figure 11.

Table 3. The parameters of the 2D model. The depth is shown in the time domain, and the impedance is calculated by multiplying density and velocity.

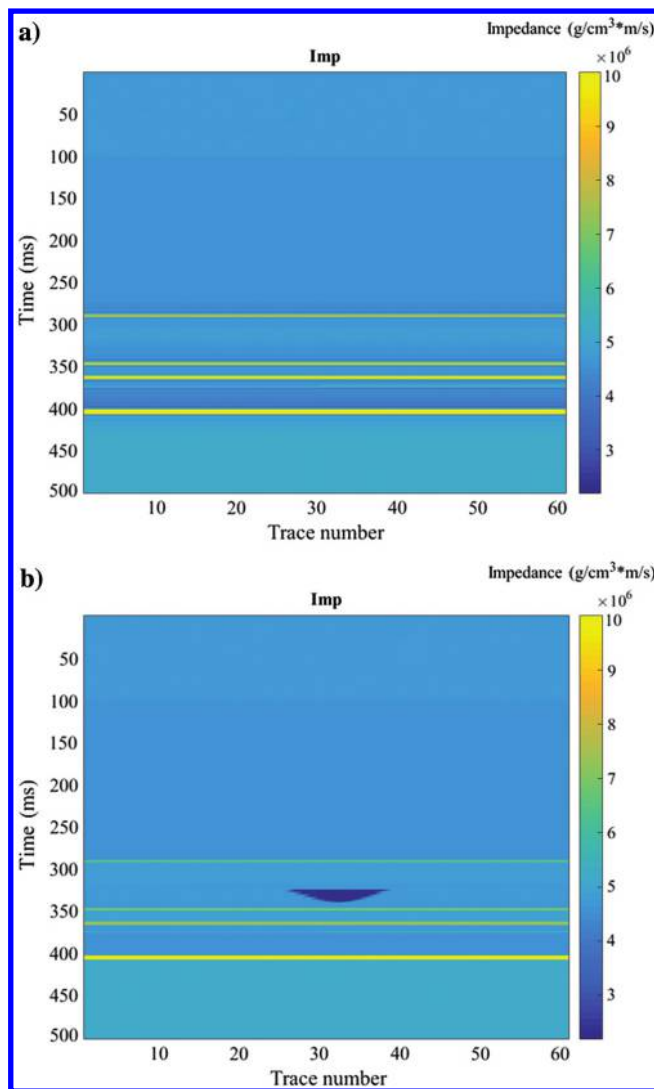|	Time (ms)	Impedance (g/cm$^3 \cdot$ m/s)
Layer 1	0–119	4670
Layer 2	119–306	4590
Layer 3	306–335	4780
Layer 4	335–360	4670
Layer 5	360–377	4910
Layer 6	377–381	7390
Layer 7	381–418	4520
Layer 8	418–423	10,050
Layer 9	423–500	5170
Steam chamber	325–338	1970

Figure 13. (a) The geologic model of the baseline survey and (b) the geologic model of the monitor-line survey. These two models show the geologic models before and after steam injection. A low-impedance zone occurs after steam injection, which is caused by the hot steam reducing the oil sands' velocities and densities. The color bar shows the value of the impedance.
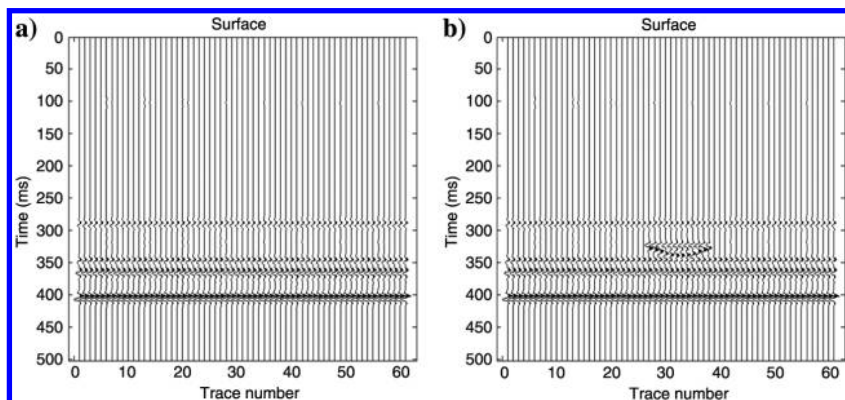

Figure 14. (a) Synthetic surface seismic of the baseline survey and (b) synthetic surface seismic of the monitor-line survey. The synthetic traces are generated by convolving the reflectivities with a 75 Hz Ricker wavelet.
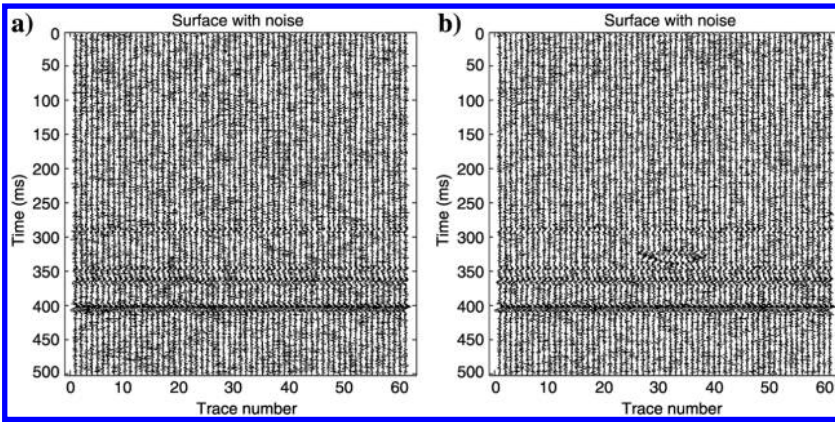
Figure 15. (a) Seismic with noise of the baseline survey, the S/N is 5; and (b) seismic with noise of the monitor-line survey, the S/N is 5. The noises are Gaussian white noise.
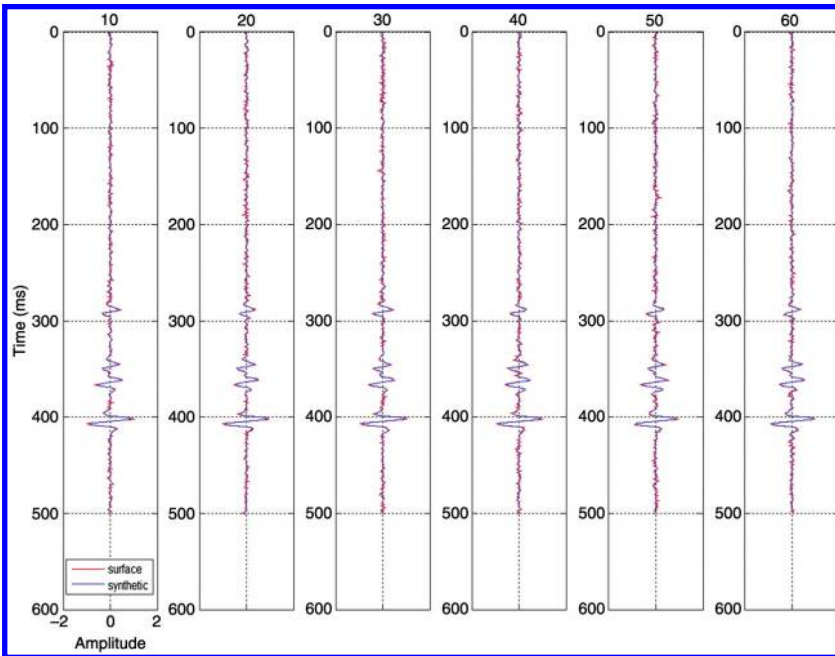

Figure 16. Inverted synthetic traces versus original seismic traces of the baseline survey. The red lines represent the original surface seismic traces and the blue lines represent the inverted synthetic traces.
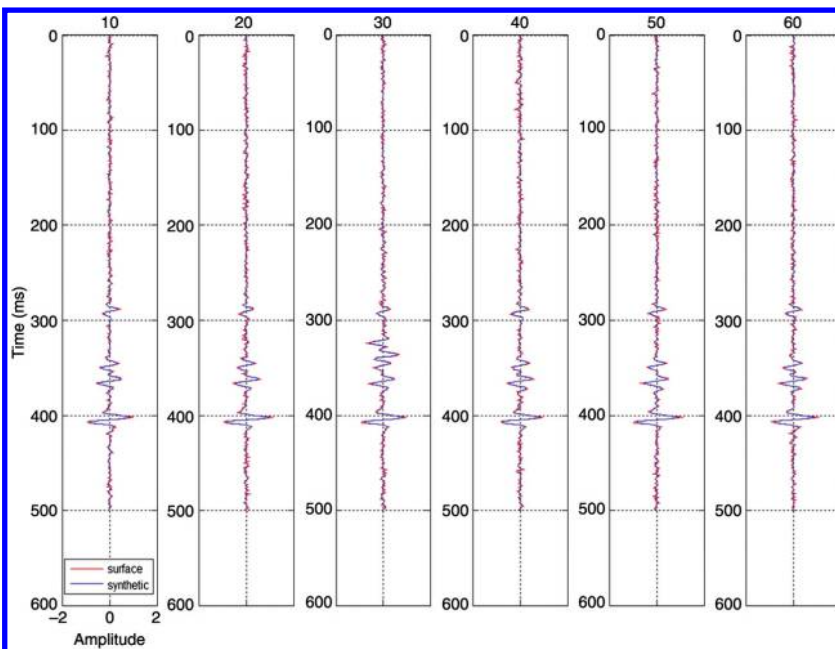

Figure 17. Inverted synthetic traces versus original seismic traces of the monitor-line survey. The red lines represent the original surface seismic traces, and the blue lines represent the inverted synthetic traces.

In Figure 9, the snapshots show the propagation of the wave energy. It can be seen in Figure 9b that weak reflection occurs at the first boundary, which is caused by the small impedance contrast between the two layers. In Figure 9c, the strong reflection appears on the top of the steam chamber due to the large impedance contrast between the overlying layer and the steam chamber. Moreover, the original wavefront shows a time lag when passing the steam chamber because of the low velocity of the steam chamber. In Figure 9d, beneath the steam chamber, there are downgoing waves originating from the steam chamber. These waves are first reflected from the bottom of the steam chamber and then reflected from the top of the steam chamber. As shown in Figure 10, the waves (⑦ and ⑧) generated due to steam chamber are quite clear and obvious. In Figure 11, the anomaly is quite evident around the steam chamber (240–380 m and 320–330 ms). On the top of the steam chamber, there are strong negative reflections, and beneath the steam chamber, the wave energy is quite weak, owing to the shielding effect of the steam chamber. This anomaly indicates that the change of the reservoir due to steam injection can lead to visible change on seismic profile.

Bayesian inversion

Time-lapse inversion is an effective tool for reservoir characterization and fluid monitoring, and many people have done research on it (Sarkar et al., 2003; Zhang et al., 2006; Lafet et al., 2009). Different methods may work for different data. Based on our data, we performed a modified-Cauchy prior constraint-based time-lapse inversion, which is based on Bayesian inference theory.

According to Bayesian inference theory, the posterior probability can be represented as the multiplication of the prior probability and likelihood function (Ulrych et al., 2001; Buland and Omre, 2003; Tarantola, 2005), which is shown in equation 3:

$$p(x|d) = \frac{p(x)p(d|x)}{\int p(x)p(d|x)dx} \propto p(x)p(d|x), \qquad (3)$$

where $p(x)$ is the prior probability density function of random variable x, $p(d|x)$ is the likelihood function, and $p(x|d)$ is the posterior probability.

There are various prior distributions, and commonly used distributions are Gaussian and Cauchy distributions (Youzwishen, 2001; Danilo, 2008), as shown in equations 4 and 5.

The Gaussian distribution is shown as

$$p(x) = \frac{1}{\sqrt{2\pi}\sigma} e^{\frac{-(x-\mu)^2}{2\sigma^2}}, \qquad (4)$$

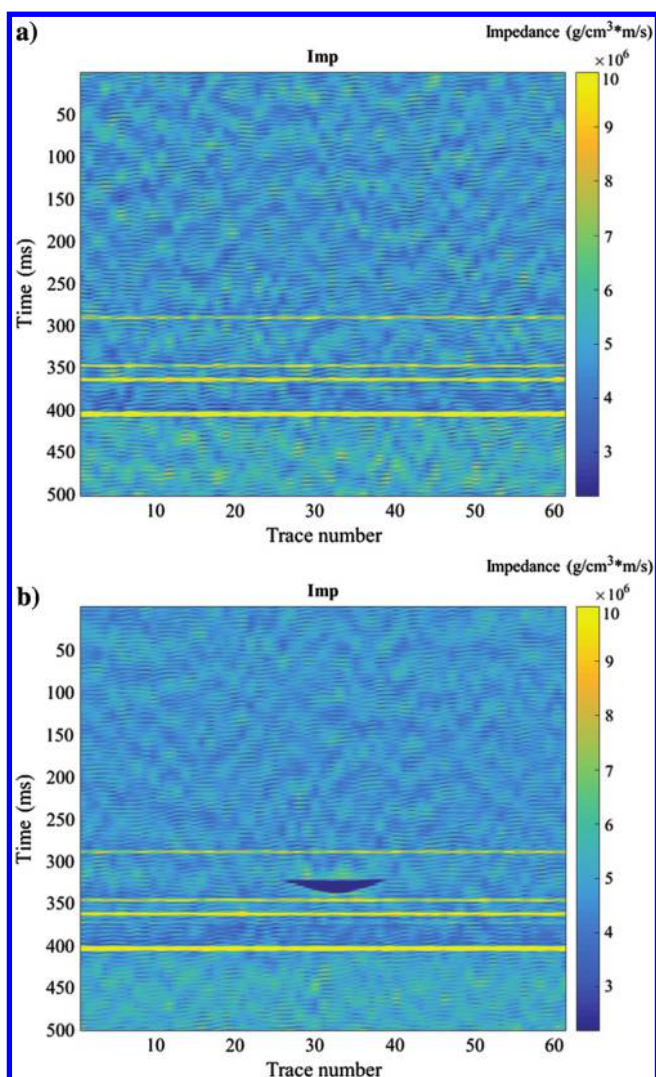where μ is the mean value and σ is the standard deviation.

Figure 18. (a) Inverted impedance of the baseline survey and (b) inverted impedance of the monitor-line survey. The color bar shows the value of the impedance.
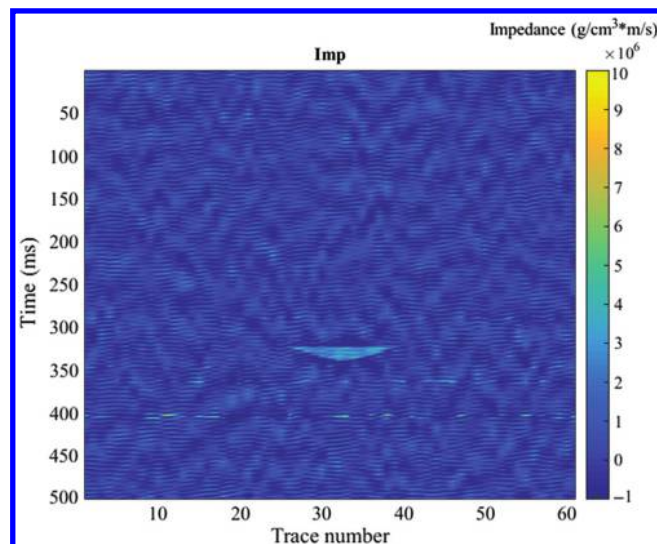

Figure 19. Impedance change between baseline and monitor-line surveys. It is obtained by subtracting monitor-line impedance from baseline impedance. Only the steam chamber has a positive anomaly, whereas the other areas seldom show any changes.

The Cauchy distribution is shown as

$$f(x; x_0, \gamma) = \frac{1}{\pi} \left[\frac{\gamma}{(x - x_0)^2 + \gamma^2} \right], \tag{5}$$

where x_0 is the location parameter and γ is the scale parameter.

We use a modified-Cauchy distribution (Cao et al., 2009; Yuan and Han, 2013a; equation 6):

$$f(x; x_0, \gamma) = \frac{1}{\pi \gamma} e^{\frac{-(x-x_0)^2}{\gamma^2 + (x-x_0)^2}}. \tag{6}$$

To identify the difference between these three distributions, a comparison of them is performed and shown in Figure 12. Figure 12a suggests that the modified Cauchy has long-tail distribution characteristic, which can help to realize the sparseness of the reflectivities. And the larger tail value enables the modified-Cauchy distribution to better protect the sparse reflectivities (Zhang et al., 2008; Cao et al., 2009). More importantly, compared with the Gaussian and Cauchy distributions, the modified-Cauchy distribution fits better with the statistical reflectivities from well logs in Figure 12b, illustrating its practicability.

If we assume that the noise in surface seismic data is normally distributed (Tarantola, 2005), of which the mean value is zero and deviation is σ_n^2, then the likelihood function of reflectivity $p(d|x)$ can be represented in the form of the noise distribution, as shown in equation 7:

$$P(d|x) = P(n) = \frac{1}{(2\pi\sigma_n^2)^{N/2}} \exp\left\{ \frac{-(d - Gx)^T(d - Gx)}{2\sigma_n^2} \right\}, \tag{7}$$

where d is the surface seismic data, n is the noise, G is the surface wavelet matrix, and σ_n is the standard deviation of noise. Then, the posterior probability can be calculated and Bayesian inversion can be performed.

Synthetic test

To test the effectiveness of the Bayesian inversion on 4D seismic, a synthetic test of the 4D-2D experiment is carried out. Figure 13a shows the baseline model, and Figure 13b shows the monitor-line model. The two models have same layers, except that the monitor-line model has a steam chamber caused by steam injection. The models have traces from 1 to 61, and the time depth ranges from 0 to 500 ms. The information of the geologic models (in Table 3) is similar to the information in Figures 7 and 8, but it is in time domain and the impedance is already calculated. Then, the reflectivity can be obtained, and the synthetic seismic traces can be generated by convolving the reflectivity with a wavelet (75 Hz Ricker wavelet), as shown in Figure 14. To test the robustness of the method, Gaussian white noise is added and the signal-to-noise ratio (S/N) equals five, which is shown in Figure 15.

Afterward, the Bayesian inversion is applied on baseline seismic and monitor-line seismic, respectively. Figures 16 and 17 show the inverted traces of baseline and monitor-line surveys, and Figure 18 shows the corresponding impedance. To better detect the steam chamber, subtraction between the baseline and monitor-line impedance is performed, and the result is shown in Figure 19.

In Figures 16 and 17, the inverted synthetic traces correlate very well with the original seismic traces. This matches the overall trends and specific details of the original seismic traces, especially at large sparse reflectivities because the modified-Cauchy prior constraint allows better protection of the sparse strong reflections. For the
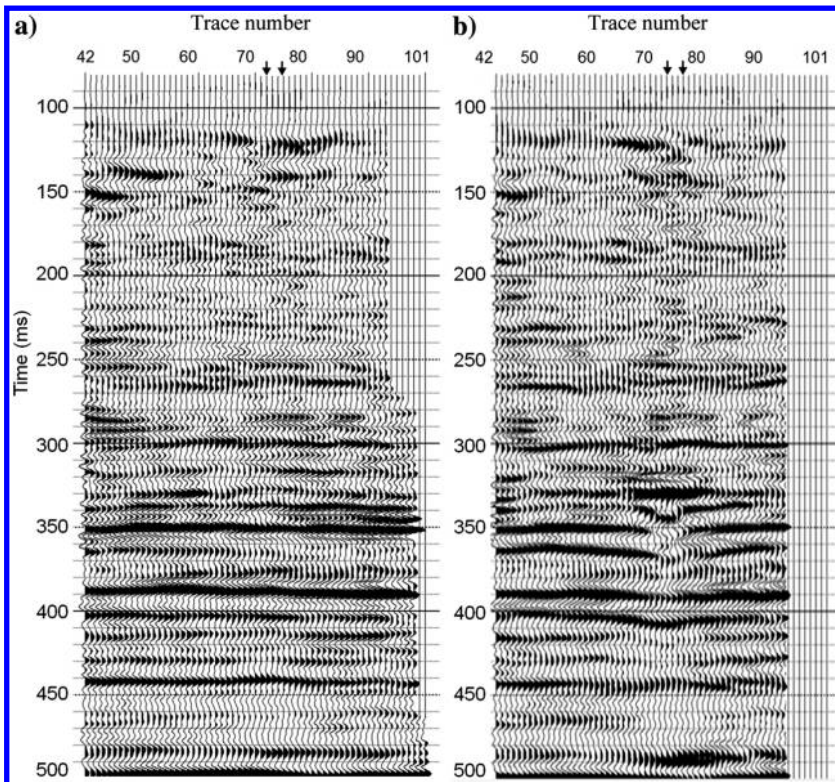

Figure 20. (a) The seismic profile of the baseline survey and (b) the seismic profile of the monitor-line survey. Most of the seismic events are consistent from baseline to monitor-line surveys, except that at approximately 320–340 ms at trace 64–84, the monitor-line seismic shows strong reflections and the events at approximately 330–350 ms were dented, which is caused by the steam injection reducing the reservoir's impedance and velocity. The black arrows on top indicate the well locations.

baseline and monitor-line seismic, there are few errors between the original seismic and the inverted synthetic traces.

For the inverted impedance in Figure 18, the layers are well-recovered and the reflection boundaries are clear. The steam chamber is also well-characterized, and the shape is the same as the original model. Figure 19 shows the result of the baseline impedance minus the monitor-line impedance, and the steam chamber is characterized as the zone with positive values. It is obvious that only the steam chamber has the anomaly and all the other areas seldom show any

value change, indicating that the method can effectively detect the steam chamber.

RESULTS

The study area is located at the Western Canadian sedimentary basin, which covers a vast area and contains massive heavy oil sands. The data contain one line for baseline and monitor-line surveys. The survey contains 61 traces, ranging from trace 42 to 102 with a 10 m trace interval. Two wells (#1 and #2) are available along the line. One well is the steam injection well, which is close to trace 74, and the other well is at trace 77.

The seismic profiles of the baseline and monitor-line surveys are shown in Figure 20. It can be found that the monitor-line survey shows an obvious difference from the baseline survey at approximately 320–340 ms at trace 64–84, suggesting the zone affected by steam injection. The events around the steam-washed zone (330–350 ms) are dented, indicating a longer traveltime at the zone, which is caused by the steam injection reducing the oil sands' velocities. Moreover, the strong seismic amplitude anomaly appears approximately 320 ms, owing to the huge changes in acoustic impedance, which is
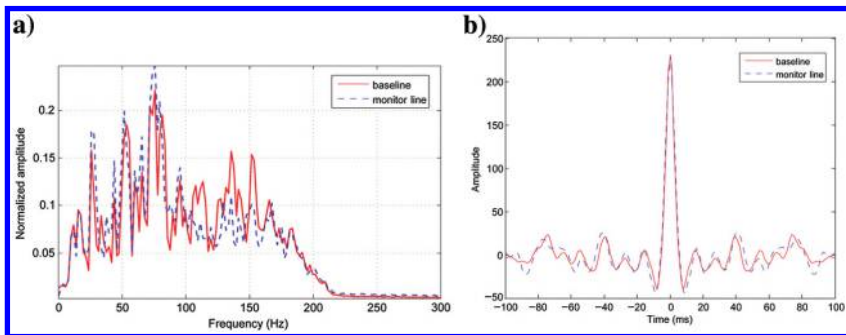

Figure 21. (a) The spectrum and (b) wavelets of baseline and monitor-line surveys. The frequency band ranges from 0 to 200 Hz for baseline and monitor-line surveys. But the high-frequency information (100–200 Hz) of monitor-line survey is attenuated. The wavelets of the baseline and monitor-line surveys are similar with only a little discrepancy in side lobes.
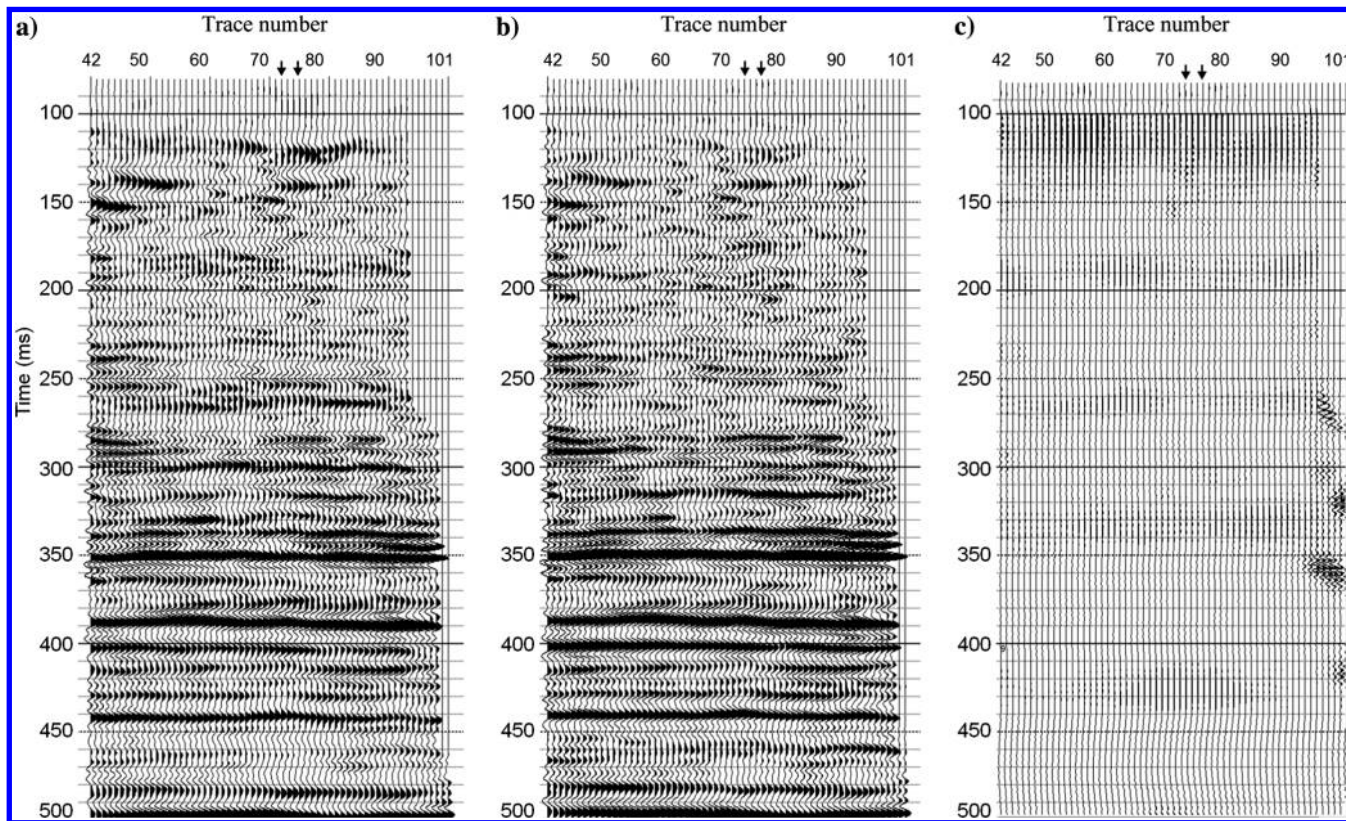

Figure 22. (a) The original seismic traces of baseline survey. (b) The synthetic traces. (c) The errors between original seismic and synthetic traces. The synthetic traces are quite similar as original surface seismic traces with consistent events and the errors are small. The black arrows on top indicate the well locations.

also caused by the steam injection reducing the oil sands' velocity and density.

To make a further analysis, wavelet extraction is implemented through the self-correlation method (Berkhout, 1977). The frequency spectrums and extracted wavelets are shown in Figure 21. It can be seen that the wavelets are similar, with little discrepancy in the side lobes. However, the frequency spectrum displays some discrepancy. The baseline survey has a frequency band from 0 to 200 Hz and the dominant frequency is 75 Hz. In comparison, the high-frequency part (100–200 Hz) of the monitor-line spectrum is attenuated because the fluid mixture inside the steam chamber can cause intense attenuation to the seismic energy, especially the high-frequency information. The frequency attenuation also justifies the influence of steam injection on the reservoir properties.

The inversion results of the baseline and monitor-line surveys are displayed in Figures 22 and 23, respectively. In Figure 22, the synthetic traces are quite similar to the original seismic traces and the errors are small. Figure 23 shows similar results for monitor-line survey, demonstrating the effectiveness of the modified-Cauchy prior constraint-based inversion. Figure 24 displays the inverted impedance, and Figure 25 shows the single-trace comparison of the impedance.

In Figure 24, it can be seen that the clastic layer at approximately 353 ms is clear and consistent, and the layer between 320 and 330 ms generally shows low impedance, indicating it is the oil sands layer. However, the appearance of the steam chamber makes the impedance apparently smaller between traces 66 and 76 on the monitor-line survey, which can also be found in Figure 25. In Figure 25, the monitor-line impedance is smaller than the baseline impedance on traces 66 and 76 between 320 and 330 ms because these two traces cross the
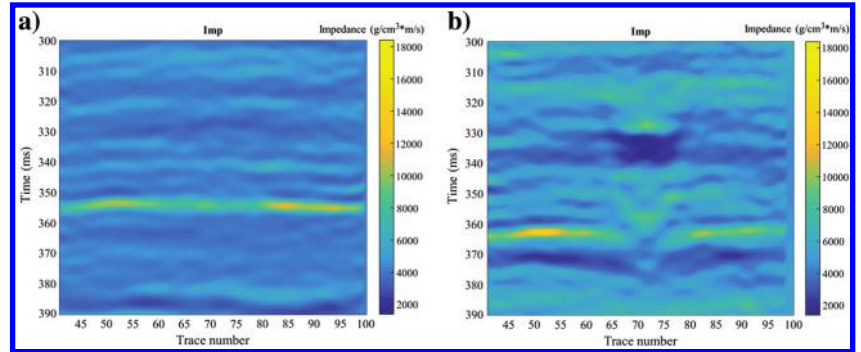

Figure 24. (a) Inverted impedance of the baseline survey. (b) Inverted impedance of the monitor-line survey. Hampson-Russell software is applied for the display. The color bar shows the value of the impedance. The impedance between the baseline and monitor line is consistent. The low-impedance layer between 320 and 330 ms is the oil sands layer, and the extremely low-impedance zone in he monitor-line survey between traces 66 and 80 is the steam chamber zone. The black arrows on top indicates the well locations.
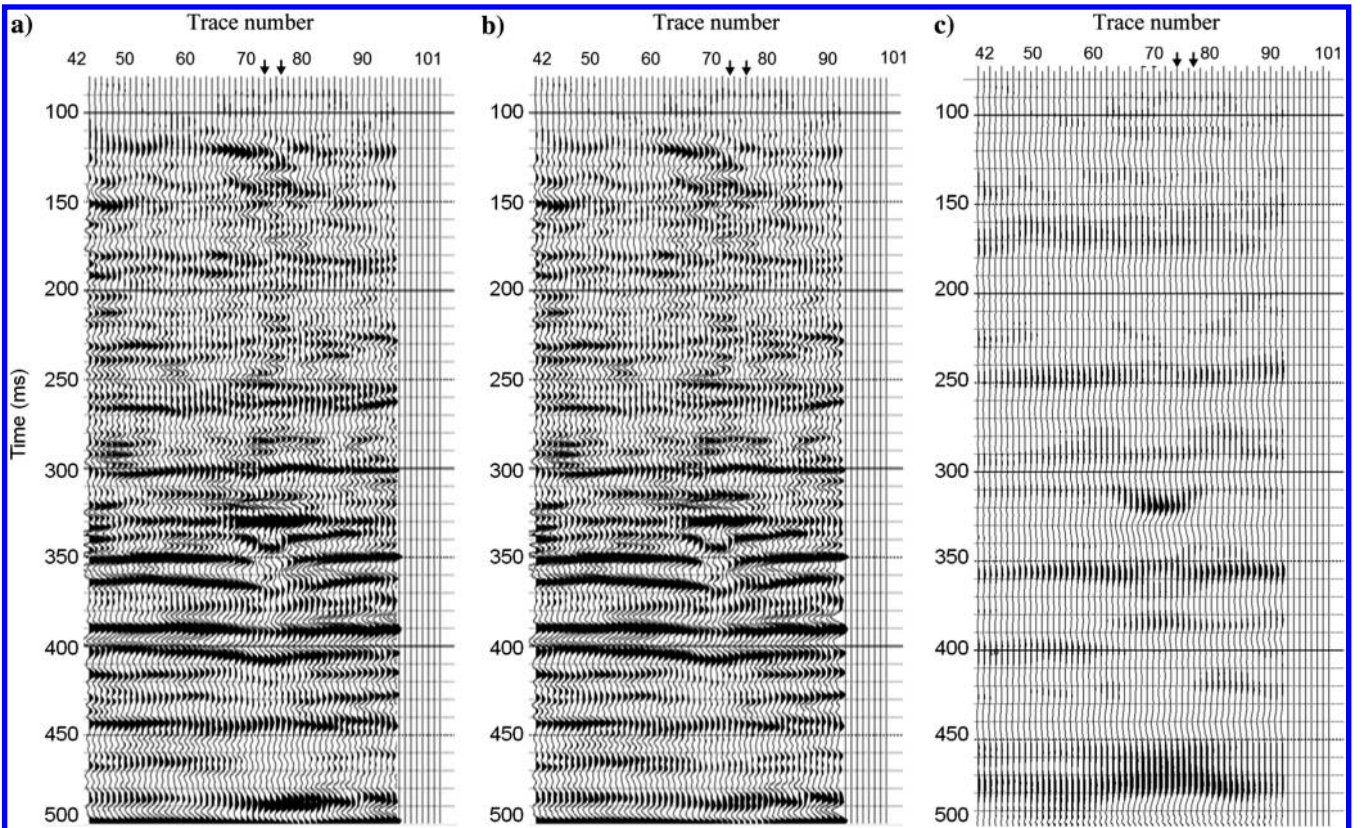

Figure 23. (a) The original seismic traces of the monitor-line survey. (b) The synthetic traces. (c) The errors between original seismic and synthetic traces. The synthetic traces are quite similar to the original surface seismic traces with consistent events, and the errors are small. The black arrows on top indicate the well locations.

steam chamber. The impedance difference is achieved by subtracting the baseline and monitor-line impedance, and the results are shown in Figure 26.

In Figure 26, it is clear that the steam chamber zone has a substantial impedance change (at approximately 20%), whereas most of the other areas do not show much change, demonstrating that the steam chamber can cause great changes to the reservoir impedance, which correlates well with our previous analysis.

Because the temperature of the reservoir changes from the in situ temperature to the injected steam temperature, the reservoir impedance must be between the impedance at the in situ temperature and the steam temperature. Given that the impedance under different temperatures is already predicted in Figure 5, based on the relative change of the impedance, the temperature can be inverted through equation 8:

$$T = \begin{cases} T_v - (I_* - I_v)\frac{T_v - T_{\text{in situ}}}{I_{\text{in situ}} - I_v}, & \text{if } I_* > I_v, \\ T_v & \text{if } I_* < I_v \end{cases} \quad (8)$$
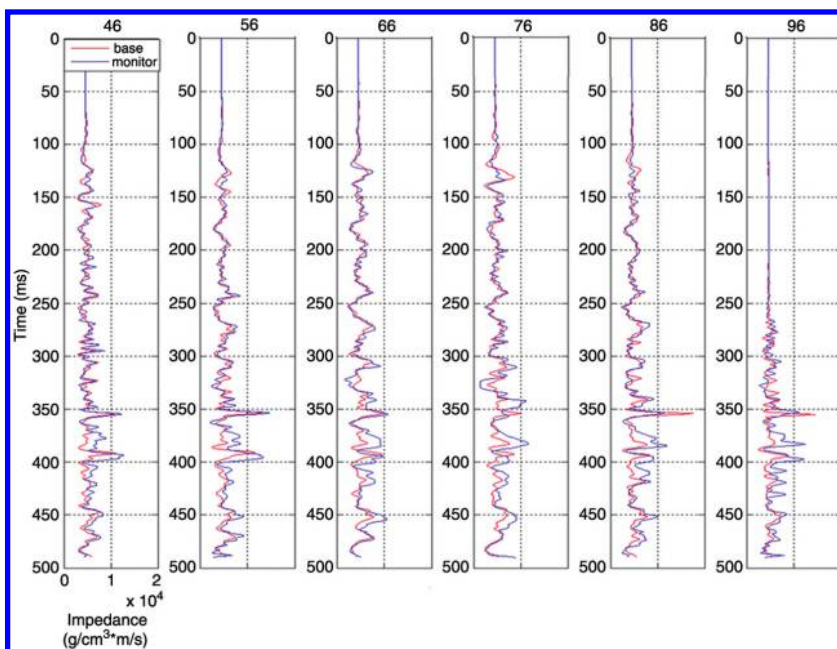
where I_* is the inverted impedance, I_{insitu} is the impedance of in situ rocks, and I_v is the impedance of the rock at the boiling point (vapor point). In this study, the in situ temperature is 12°C and the boiling point is 210°C; therefore,

$$T_{\text{in situ}} = 12, \quad (9)$$

$$T_v = 210, \quad (10)$$

$$I_{\text{in situ}} = I_{12}, \quad (11)$$

$$I_v = I_{210}, \quad (12)$$

where I_{12} is the measured impedance at 12°C and I_{210} is the impedance at 210°C, both of which can be obtained from Figure 5. The inverted temperature distribution map is shown in Figure 27.

In Figure 27, the steam chamber is quite evident with steam spreading widely on top and oil being produced on bottom. The red color indicates its high temperature, and the temperature inside the steam chamber is higher than 210°C, which agrees with the production report. Hence, this method of inverting temperature from impedance is effective.
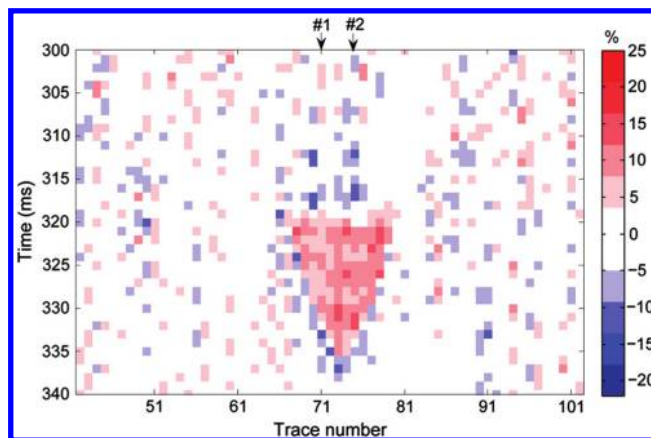

Figure 26. Difference between impedance of the baseline and monitor-line surveys. The difference is shown in percent change as the color bar shows. The difference is obtained by subtracting the monitor-line impedance from the baseline impedance and then dividing by the baseline impedance. The steam chamber is quite clear and shows more than 20% change in impedance. The black arrows on top indicate the well locations. Label #1 is the well at trace 74, and label #2 is the well at trace 77.

Figure 25. Trace comparison between baseline and monitor-line impedances. Most of the impedances are consistent, except that for traces 66 and 76 approximately 320–330 ms, the impedances are obviously lower, indicating the effect of the steam chamber because these two lines cross the steam chamber.

Velocity estimation

Because the data are poststack seismic data, it is impossible to invert the velocity directly; all that we can get is the P-wave impedance. However, based on some empirical equations, the relations between impedance and velocities can be established. Then, by combining the inverted P-wave impedance, the velocity can be derived.
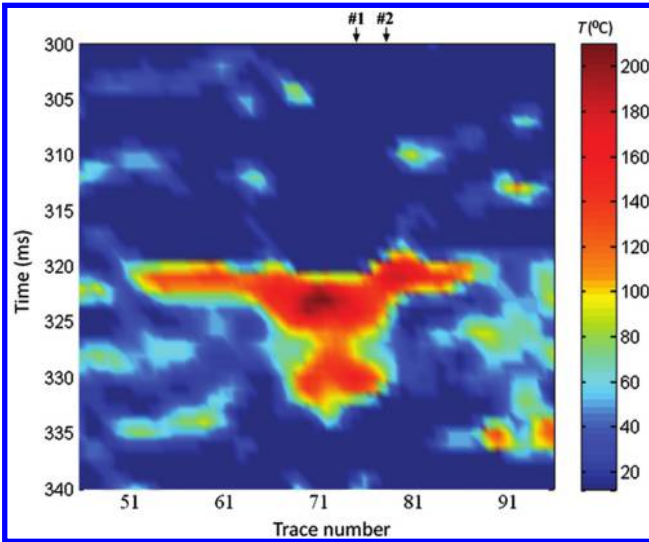

Figure 27. The inverted temperature distributions. The color bar indicates the temperature: The red color corresponds to high temperatures, and the blue color corresponds to low temperatures. The dark red color inside the steam chamber suggests that the temperature of the steam injection is greater than 210°C. The shape of the steam chamber suggests that the steam spreads horizontally on top of the steam chamber, which is reasonable for a steam chamber. The black arrows on top indicate the well locations.
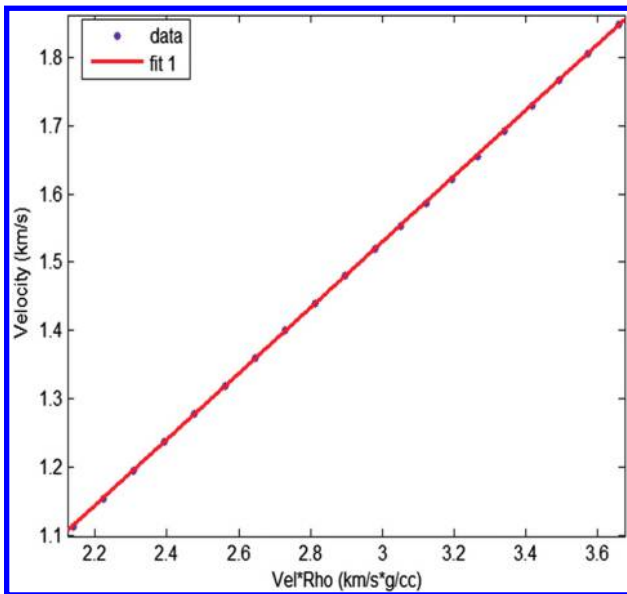

Figure 28. The velocity versus the impedance of laboratory-measured data. The blue dots are the laboratory-measured data, and the red line is the fitting line between velocity and impedance. It is clear that the velocity correlates well with the impedance linearly.

The Lindseth equation is an empirical linear relation between velocity and impedance, which was derived by Lindseth (1979). The equation is shown in equation 13:

$$v = 0.308\rho v + 3460, \tag{13}$$

where the velocity v is in units of ft/s, and density ρ is in units of g/cm^3. However, if considering velocity in km/s, the equation will change to

$$v = 0.308\rho v + 1.055. \tag{14}$$

Then, the Lindseth equation can be generalized as

$$v = c\rho v + d = cI + d, \tag{15}$$

where I is the impedance that can be obtained through the inversion results.

Using a least-squares linear fit for equation 15, the parameters of c and d are derived (c is 0.4827 and d is 0.0811). Also, the fitting of the equation and the laboratory data are shown in Figure 28.

In Figure 28, it can be found that with the obtained parameters, the modified equation matches the laboratory data well. However, this fitting is only for the laboratory data. To make the equation
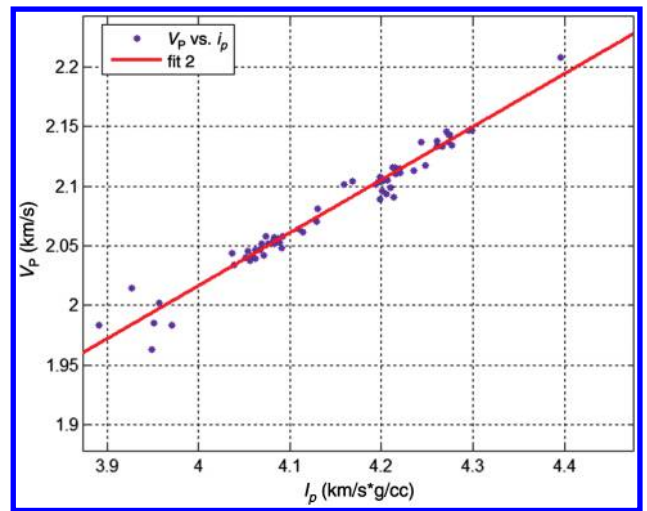

Figure 29. The velocity versus the impedance of well-log data. The blue dots are the well-log data, and the red line is the fitting line between velocity and impedance. The velocity and impedance correlate linearly, and the line fits the data well.

Table 4. The parameters of modified-Lindseth equation obtained by fitting the laboratory and the well-log data. The parameters are close, which may suggest that the true relation between velocity and impedance is actually in the range of the parameters.

	Laboratory	Well	Middle
c	0.4827	0.4442	0.4634
d	0.0811	0.2392	0.1602

more practical, the parameters are also generated through well logs (c is 0.4442 and d is 0.2392) and the fitting is shown in Figure 29. It is quite clear that the equation matches the well data and the deviations are small.

The comparison of equations obtained through laboratory data and well log is shown in Table 4 and Figure 30. It can be seen that the parameters are analogous, and both the equations are close and
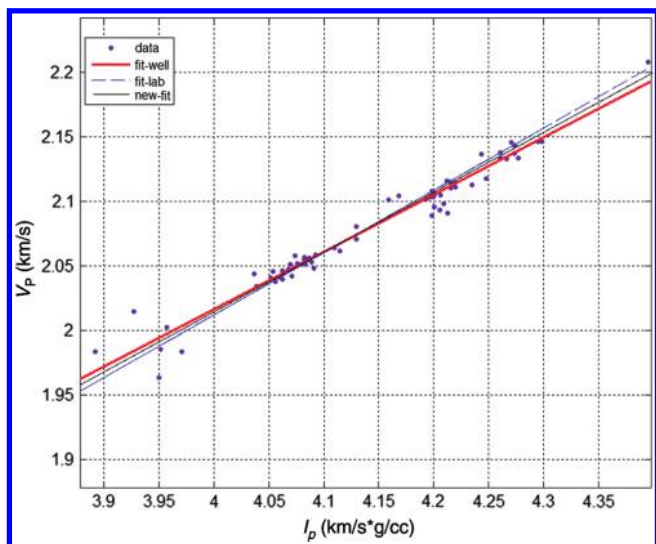

Figure 30. Comparison of modified-Lindseth equations obtained from laboratory and well-log data. The blue dots are the well-log data; the dashed blue line is the modified-Lindseth equation from laboratory data; and the red line is the modified-Lindseth equation from well-log data. The two lines are close, and they both match the data.
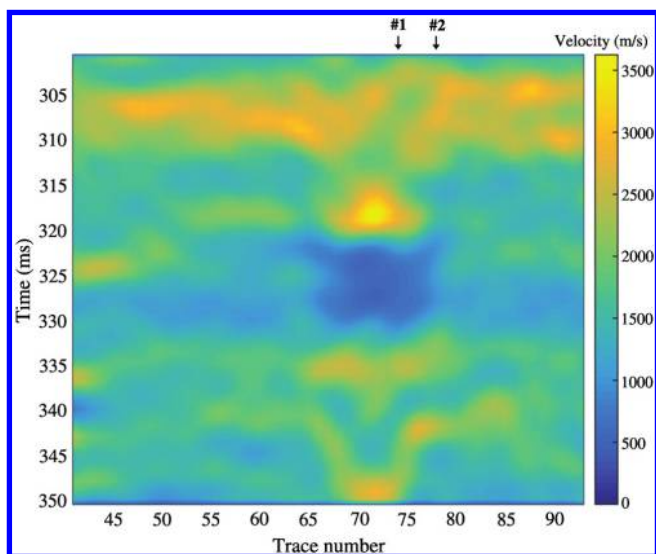

Figure 31. The inverted velocity. It is obtained by combining the modified-Lindseth equation and the inverted seismic impedance. The color bar shows the value of velocity. The layer between 320 and 330 ms generally has low velocity at less than 1.9 km/s, and the steam chamber has even lower velocity at less than 1.3 km/s, indicating the influence of steam. The black arrows on top indicate the well locations.

match the data. Considering the two equations, we take the middle line (in Figure 30 and Table 4) between them as our final equation:

$$v = 0.4634I + 0.1602, \qquad (16)$$

where the velocity v is in units of km/s and impedance I is in units of g/cm^3·km/s. Then, based on the inverted impedance in Figure 24, the velocity can be obtained in Figure 31.

In Figure 31, it is obvious that the velocity shows a quite-low-value zone, which correlates well with the impedance in Figure 24, demonstrating that the low-value zone is the steam chamber. Moreover, the velocity inside the steam chamber is between 1.1 and 1.2 km/s inside the steam chamber, suggesting the existence of steam.

CONCLUSIONS

On the basis of the above calculations and analysis, we can draw several conclusions. The steam injection can cause the velocities and densities of heavy oil reservoir to drop, and thus the impedance also drops. The decrease of velocities inside the steam chamber can lead to longer traveltimes, and thus seismic events are dented on seismic profiles. The small impedance can cause large reflectivities and strong amplitudes. The forward modeling reveals that the top and bottom of the steam chamber can also generate complex reflections that can be identified on the wavefield snapshots and angle gathers.

The inversion method with a modified-Cauchy prior constraint works well on the 2D model and field data, and the errors between the original and synthetic traces are small. The inverted impedance successfully shows the low impedance of the oil sands layer and even the lower impedance of the steam chamber. Also, the subtraction between the baseline and monitor-line impedance tells us the amount of change in impedance before and after steam injection, which is more than 20%.

The temperature-distribution map is obtained through combining the rock-physics relation and the inverted impedance. The map clearly shows the shape and temperature distribution of the steam chamber. The temperature is more than 210°C inside the steam chamber, indicating the existence of steam. Based on the Lindseth empirical equation, a new equation of the oil sands' velocity is established. Then, by combining the inverted impedance, the velocity of the reservoir is derived. The velocity map correlates well with the impedance, illustrating the effectiveness of the method. Because the parameters of the modified Lindseth equation are determined through fitting the laboratory data and well data, the equation would be more reliable if more data are available.

ACKNOWLEDGMENTS

REFERENCES

Berkhout, A. J., 1977, Least-squares inverse filtering and wavelet deconvolution: Geophysics, **42**, 1369–1383, doi: 10.1190/1.1440798.

Bianco, E., S. Kaplan, and D. Schmitt, 2008, Seismic rock physics of steam injection in bitumen oil reservoirs: The Leading Edge, **27**, 1132–1137, doi: 10.1190/1.2978975.

Buland, A., and H. Omre, 2003, Bayesian wavelet estimation from seismic and well data: Geophysics, **68**, 2000–2009, doi: 10.1190/1.1635053.

Butler, R. M., 1990, Thermal recovery of oil and bitumen: Prentice Hall PTR.

Cao, D., X. Yin, and F. Zhang, 2009, Joint inversion of 3D seismic VSP and crosswell seismic data: 79th Annual International Meeting, SEG, Expanded Abstracts, 2373–2377.

Danilo, R., 2008, Stochastic sparse-spike deconvolution: Geophysics, **73**, no. 1, R1–R9, doi: 10.1190/1.2790584.

Diao, S., J. Li, and D. Tang, 2003, Time-lapse seismic-forward modeling based on black-oil model: Progress in Exploration Geophysics, **26**, 19–23.

Dumitrescu, C. C., and L. Lines, 2009, Case study of a heavy-oil reservoir interpretation using V_P/V_S ratio and other seismic attributes: 79th Annual International Meeting, SEG, Expanded Abstracts, 1765–1769.

Eastwood, J., P. Lebel, and A. Dilay, 1994, Seismic monitoring of steam-based recovery of bitumen: The Leading Edge, **13**, 242–251, doi: 10.1190/1.1437015.

Isaac, J. H., 1996, Seismic methods for heavy-oil reservoir monitoring: Ph. D. thesis, University of Calgary.

Kato, A., 2010, Reservoir characterization and steam monitoring in heavy oil reservoirs: Ph.D. thesis, University of Houston.

Kendall, R., 2009, Using time lapse seismic to monitor the THAI™ heavy-oil production process: 79th Annual International Meeting, SEG, Expanded Abstracts, 3954–3958.

Lafet, Y., B. Roure, P. M. Doyen, and H. Buran, 2009, Global 4-D seismic inversion and time-lapse fluid classification: 79th Annual International Meeting, SEG, Expanded Abstracts, 3830–3834.

Li, G. P., G. Purdue, S. Weber, and R. Couzens, 2001, Effective processing of nonrepeatable 4-D seismic data to monitor heavy-oil SAGD steam flood at East Senlac, Saskatchewan, Canada: The Leading Edge, **20**, 54–62, doi: 10.1190/1.1438878.

Lindseth, R. O., 1979, Synthetic sonic logs — A process for stratigraphic interpretation: Geophysics, **44**, 3–26, doi: 10.1190/1.1440922.

Marcano, N., 2013, The geochemical toolbox to monitoring thermal recovery operations in oil sands and heavy oil reservoir: Presented at the Integration GeoConvention.

Meyer, R., and E. Attanasi, 2003, Heavy oil and natural bitumen: Strategic petroleum resources: U.S. Geological Survey.

Nakayama, T., A. Takahashi, L. Skinner, and A. Kato, 2008, Monitoring an oil-sands reservoir in northwest Alberta using time-lapse 3D seismic and 3D P-SV converted-wave data: The Leading Edge, **27**, 1158–1175, doi: 10.1190/1.2978979.

Sarkar, S., W. P. Gouveia, and D. H. Johnston, 2003, On the inversion of time-lapse seismic data: 73rd Annual International meeting, SEG, Expanded Abstracts, 1489–1492.

Schmitt, D. R., 1999, Seismic attributes for monitoring of a shallow heated heavy oil reservoir: A case study: Geophysics, **64**, 368–377, doi: 10.1190/1.1444541.

Sun, Z. D., 1999, Seismic methods for heavy-oil reservoir monitoring and characterization: Ph.D. thesis, University of Calgary.

Tarantola, A., 2005, Inverse problem theory and methods for model parameter estimation: SIAM.

Ulrych, T. J., M. D. Sacchi, and A. Woodbury, 2001, A Bayes tour of inversion: A tutorial: Geophysics, **66**, 55–69, doi: 10.1190/1.1444923.

Youzwishen, C. F., 2001, Non-linear sparse and blocky constraint for seismic inverse problems: M.S. thesis, University of Alberta.

Yuan, H., and D. Han, 2013a, A study of multiscale seismic data joint inversion method: 83rd Annual International Meeting, SEG, Expanded Abstracts, 3169–3173.

Yuan, H., and D. Han, 2013b, Pressure and temperature effect on heavy oil sand properties: 83rd Annual International meeting, SEG, Expanded Abstracts, 2984–2988.

Yuan, H., D. Han, and W. Zhang, 2016, Heavy oil sands measurement and rock physics modeling: Geophysics, **81**, no. 1, D57–D70, doi: 10.1190/geo2014-0573.1.

Zhang, F., J. Liu, and X. Yin, 2008, Blind deconvolution method based on modified Cauchy constraint: Oil Geophysical Prospecting, **43**, 391–396.

Zhang, M. Y., M. D. Sacchi, and D. R. Schmitt, 2006, Time-lapse inversion with sparseness, impedance and structural constraints: Presented at the CSPG-CSEG-CWLS Convention.

Zhang, W., G. Li, and J. Cody, 2002, Understanding reservoir architecture at Christina Lake, Alberta with crosswell seismic imaging: CSEG.

Zou, Y., L. R. Lines, K. Hall, and J. Embleton, 2004, Time-lapse seismic analysis of a heavy oil cold production field, Lioydminster, Western Canada: 74th Annual International Meeting, SEG, Expanded Abstracts, 1555–1558.

This article has been cited by:

1. Hemin Yuan, De-Hua Han, Qi Huang, Qianqian Wei, Huizhong Yan, Weimin Zhang. Steam chamber detection through seismic attributes 3796-3800. [Abstract] [References] [PDF] [PDF w/Links]
2. . Rock Physics II Complete Session 3771-3975. [Abstract] [PDF] [PDF w/Links]